

# MR image reconstruction using the learned data distribution as prior

Kerem C. Tezcan<sup>1,\*</sup>, Christian F. Baumgartner<sup>1</sup>, and Ender Konukoglu<sup>1</sup>

<sup>1</sup>Computer Vision Laboratory, ETH Zürich

\*tezcan@vision.ee.ethz.ch

December, 2017

## Abstract

**Purpose:** MR image reconstruction from undersampled data exploits priors which can compensate for missing k-space data. This has previously been achieved by using regularization methods, such as TV and wavelets, or data adaptive methods, such as dictionary learning. In this work, we propose to explicitly learn the probability distribution of MR image patches and to constrain patches to have a high probability according to this distribution in reconstruction, effectively employing it as the prior in reconstruction.

**Methods:** We use variational autoencoders (VAE) to learn the distribution of MR image patches. This high dimensional distribution is modelled by a latent parameter model of lower dimensions in a non-linear fashion. We develop a reconstruction algorithm that uses the learned prior in a Maximum-A-Posteriori estimation formulation. We evaluate the proposed reconstruction method with T1 weighted images acquired at 3T and compare it to existing alternatives. We also apply our method on images with white matter lesions.

**Results:** Visual evaluation of the samples drawn from the learned model showed that the VAE algorithm was able to approximate the distribution of MR image patches. Furthermore, the reconstruction algorithm using the approximate distribution produced qualitatively better results compared to previous methods. Quantitative evaluation confirmed the visual inspection. The proposed technique achieved RMSE, CNR and CN values of 2.77%, 0.43, 0.11 and 4.29%, 0.43, 0.11 for undersampling ratios of 2 and 3, respectively. It outperformed other evaluated methods in terms of used metrics. In the experiments on images with white matter lesions, the method faithfully reconstructed the lesions.

**Conclusion:** We introduced a novel method for MR reconstruction, which takes a new perspective on regularization by learning priors. Results suggest the method compares favorably against TV and dictionary based methods as well as the neural-network based ADMM-Net in terms of the RMSE, CNR and CN and perceptual image quality and can reconstruct lesions as well.

**Keywords:** Reconstruction, MRI, prior probability, MAP estimation, machine learning, variational inference, deep learning

## 1 Introduction

Acquisition time in magnetic resonance (MR) imaging is directly related to the number of samples acquired in k-space. For high quality images, a large number of samples, and therefore long acquisition times are necessary. Many methods exploiting different properties of k-space, image space as well as the the encoding power of multiple receive antennae have been proposed to reduce the acquisition time. Some of these methods found widespread use in clinical practice, due to their reliability and reproducibility. Notable examples include partial Fourier/echo imaging [1] which exploit Hermitian symmetry of k-space representations of objects and sensitivity encoding (SENSE) [2], which utilizes parallel receive hardware.

On the other hand, a substantial amount of effort went into the investigation of reconstruction methods from randomly or regularly undersampled k-space acquisitions. Former approach was primarily motivated by the compressed sensing framework where the incoherence between k-space sampling and some sparsifying transform was exploited to achieve theoretically exact reconstruction [3]. Similarly, regular undersampling schemes and corresponding reconstruction algorithms were extensively investigated [4]. The common aspect of these two approaches is that they both are interested in inverting an underdetermined system of equations. To achieve this, both methods aim to find good regularizers to overcome the ill-posedness of the inversion problem.

The regularizers employed in both approaches can essentially be viewed as introducing prior information to the reconstruction problem. For compressed sensing based methods the main idea is to use i) a transform, which projects the signal to a space, where the signal is sparse, ii) a norm to find sparse solutions [5, 6]. The transforms that are commonly used are total variation [3], wavelet decomposition [7], sparse-low rank decomposition [8]. Similarly, the  $\ell_1$  norm is used as the sparsity inducing norm. For methods employing regular undersampling, the main idea is to acquire a low resolution image in parallel and to use the information from this image to make the inversion problem well-posed [9]. The idea is extended by use of additional transforms (such as principal component analysis (PCA) [10, 11]) on the low resolution information, to improve the regularizer.

Recently, researchers started to employ deep neural networks (DNN) [12] for MR reconstruction inspired by its success in computer vision and medical image analysis [13]. DNNs success partially lies in the fact that networks can learn complex mappings from input to output and the mappings can be efficiently trained using large number of examples, i.e. training data sets, and back-propagation.

In the related literature there are two main approaches for applying DNNs to the reconstruction problem. The first is to use the networks as a mapping from undersampled images to their fully sampled versions [14]. In this approach, networks are trained using pairs of images, undersampled and fully sampled, and when deployed, an undersampled image is simply fed into the network to obtain its reconstruction at the output. This approach does not have any explicit data consistency term and cannot guarantee this property at test time. To overcome this limitation, in [15] the authors introduce a deep cascaded network. Here a block of convolutional neural network (CNN) is followed by a data consistency term and this structure is repeated multiple times. This guarantees consistency with measured data also at test time while the CNNs perform de-aliasing.

The second approach is to use the efficient trainability of the networks to improve existing algorithms. In [16] the authors show that the iterations of the alternating direction method of multipliers (ADMM) algorithm solving a dictionary based regularized reconstruction problem can be expressed as a multi-layer network. Kernels and non-linear functions are parameterized by the network. Through training the authors show that they can obtain better kernels and non-linear functions compared to the initial discrete cosine transform basis and the  $\ell_1$  norm. Both approaches suffer from specificity of training. Learned mappings, kernels and non-linearities are specific to a certain undersampling pattern and possibly field-of-view (FOV). Hence, the networks need to be retrained for each different configuration of FOV, undersampling factor and pattern, which limits wide use of these methods.

In computer vision, DNNs have also been used for approximating high dimensional probability distributions from samples through unsupervised learning. Such approximations allow generating new data samples or to estimate the likelihood of a previously unseen data point. One such approach is the variational auto encoder (VAE) algorithm [17, 18]. The VAE implements a probabilistic latent variable model, which approximates the high-dimensional data distribution by parameterizing with a lower dimensional encoding. Parameters of the model are learned from training samples. Using VAEs, it is possible to approximate the distribution of patches of MR images and compute likelihood of a previously unseen image. Furthermore, the likelihood function is differentiable since it is modelled as a neural network.

In this work we develop a probabilistic reconstruction model that uses priors learned via VAEs,

deploying them as regularizers. The approach can be used to learn the prior distribution once using fully sampled data and removes the need for retraining for each set of different sampling parameters. To achieve this we first formulate a Bayesian model of the imaging process and express the reconstruction problem as a Maximum-A-Posteriori (MAP) estimation problem. We show how some of the previous methods fit into this formulation and then present the proposed model using a VAE-learned prior. In the experiments, we first demonstrate that VAEs can approximate distribution of patches of MR images by showing examples of patches sampled from the prior, i.e. generated patches. We then show reconstruction results from the proposed model and compare with both more conventional approaches as well as recent DNN based methods.

## 2 Methods

In the first two parts of this section, we provide a brief background on Bayesian formulation of the MR reconstruction problem and the VAE algorithm. Then, starting from Section 2.3, we present our main technical contribution, that is learning priors and integrating these in the reconstruction problem.

### 2.1 Bayesian formulation of the MR reconstruction problem

The MR image is denoted as  $\mathbf{m} \in \mathbb{C}^N$ , where  $N$  is number of voxels<sup>1</sup>. The imaging operation is given by the undersampling encoding operation  $E = UFS$ , where  $S : \mathbb{C}^N \rightarrow \mathbb{C}^{N \times \gamma}$  is the sensitivity encoding operator. Here,  $\gamma$  is number of coils,  $F : \mathbb{C}^{N \times \gamma} \rightarrow \mathbb{C}^{N \times \gamma}$  is the Fourier operator and  $U : \mathbb{C}^{N \times \gamma} \rightarrow \mathbb{C}^{M \times \gamma}$  is the undersampling operator, with  $M < N$ .

Assuming complex valued zero mean normal distributed noise, denoted as  $\eta$ , the acquired data  $\mathbf{y} \in \mathbb{C}^{M \times \gamma}$  can be written as  $\mathbf{y} = E\mathbf{m} + \eta$ . That is, the data is normally distributed around a mean given as  $E\mathbf{m}$  with standard deviation  $\sigma_\eta$ . Under this noise model the data likelihood becomes

$$p(\mathbf{y}|\mathbf{m}) = N(\mathbf{y}|E\mathbf{m}, \sigma_\eta) = \frac{1}{(2\pi\sigma_\eta^2)^{M/2}} e^{\frac{1}{2\sigma_\eta^2} (E\mathbf{m} - \mathbf{y})^H (E\mathbf{m} - \mathbf{y})}, \quad (1)$$

where  $H$  denotes the Hermitian transpose. In reconstruction, we are interested in the posterior distribution  $p(\mathbf{m}|\mathbf{y})$ , i.e. the probability of the image being  $\mathbf{m}$  given the k-space measurements, which can be written using the Bayes' theorem as

$$p(\mathbf{m}|\mathbf{y}) = \frac{p(\mathbf{y}|\mathbf{m})p(\mathbf{m})}{p(\mathbf{y})}. \quad (2)$$

The common approach to model the reconstruction problem, which we will also use, is to use the MAP estimation

$$\arg \max_{\mathbf{m}} p(\mathbf{m}|\mathbf{y}) = \arg \max_{\mathbf{m}} p(\mathbf{y}|\mathbf{m})p(\mathbf{m}), \quad (3)$$

where the equality is due to  $p(\mathbf{y})$  not depending on  $\mathbf{m}$ .  $p(\mathbf{m})$  is called the prior term and represents the information one has about the fully sampled image before the data acquisition. Taking the log of both sides for ease of computation and plugging in the definition of the likelihood term yields

$$\begin{aligned} \arg \max_{\mathbf{m}} \log p(\mathbf{m}|\mathbf{y}) &= \arg \max_{\mathbf{m}} [\log p(\mathbf{y}|\mathbf{m}) + \log p(\mathbf{m})] \\ &= \arg \max_{\mathbf{m}} \left[ -\log \left( (2\pi\sigma_\eta^2)^{M/2} \right) - \frac{1}{2\sigma_\eta^2} (E\mathbf{m} - \mathbf{y})^H (E\mathbf{m} - \mathbf{y}) + \log p(\mathbf{m}) \right]. \end{aligned} \quad (4)$$

---

<sup>1</sup>In this work we focus on 2D imaging, however, the same techniques can be applied to 3D imaging and this extension will be a part of our future work.

Rewriting the likelihood and ignoring terms that do not vary with  $\mathbf{m}$  yields

$$\arg \max_{\mathbf{m}} \log p(\mathbf{m}|\mathbf{y}) = \arg \max_{\mathbf{m}} \left[ -\frac{1}{\lambda} \|E\mathbf{m} - \mathbf{y}\|_2^2 + \log p(\mathbf{m}) \right] \quad (6)$$

where we define  $\lambda \triangleq 2\sigma_\eta$ . Taking the maximum, or equivalently taking the minimum of the negative of the expression and multiplying all sides with  $\lambda$  recovers the conventional formulation of the reconstruction problem

$$\hat{\mathbf{m}} = \arg \min_{\mathbf{m}} \|E\mathbf{m} - \mathbf{y}\|_2^2 - \lambda \log p(\mathbf{m}). \quad (7)$$

From the point of view of Equation 7, regularization-based reconstruction algorithms differ in the log prior term they use. A generic prior expression can be written as  $\log p(\mathbf{m}) = \|\Psi(\mathbf{m} - \mu)\|_p$ , where  $\Psi$  is a sparsifying operator,  $\mu$  is the expected image and  $\|\cdot\|_p$  is the  $\ell$ -p norm.

For instance, forcing the image to be sparse in some domain can be expressed as assuming the data is i.i.d. according to the Laplace distribution in the domain [19, 20]. Mathematically, this is

$$p(\mathbf{m}) = |\det(\Psi)| p(\Psi\mathbf{m}) = |\det(\Psi)| \text{Lap}(\Psi\mathbf{m}|0, b) = |\det(\Psi)| \prod_i \frac{1}{2b} \exp\left(-\frac{|(\Psi\mathbf{m})_i|}{b}\right), \quad (8)$$

where we set  $\mu = 0$ , denote the matrix determinant with  $\det^2$ , use  $|\cdot|$  as the magnitude and  $i$  indexes voxels in the image. Now, taking the  $-\log$  and ignoring the terms that do not vary with  $\mathbf{m}$  we get

$$-\log p(\mathbf{m}) \propto \frac{1}{b} \sum_i |(\Psi\mathbf{m})_i| = \frac{1}{b} \|\Psi\mathbf{m}\|_1. \quad (9)$$

Setting  $b = 1/\lambda$  yields the prior term in Equation 7. Furthermore, setting  $\Psi$  as the gradient operator with first order finite differences, denoted by  $\nabla$ , corresponds to enforcing sparsity in the gradient domain recovering the basic total variation compressed sensing reconstruction

$$\hat{\mathbf{m}} = \min_{\mathbf{m}} \|E\mathbf{m} - \mathbf{y}\|_2^2 + \lambda \|\nabla\mathbf{m}\|_1.$$

Alternatively, both  $\Psi$  and  $\mu$  can be estimated using a low-resolution image of the same object [10, 22]. In this case, the prior term measures the distance of the image to the low resolution data in some transform domain, such as Fourier or PCA domains. One example for this approach is to assume a Normal prior on  $\mathbf{m}$ ,  $p(x) = N(\mu_m, \Sigma_m)$  with mean  $\mu_m$  and covariance  $\Sigma_m$ . The posterior  $p(\mathbf{y}|\mathbf{m})$  is then also a Normal distribution due to conjugacy relations and the MAP estimate is given with the posterior mean [23]

$$\begin{aligned} \mu_{post} &= \left[ \frac{1}{\sigma_\eta} E^H E + \Sigma_m^{-1} \right]^{-1} \left( \frac{1}{\sigma_\eta} E^H \mathbf{y} + \Sigma_m^{-1} \mu_m \right) \\ &= \mu_m + \left[ \frac{1}{\sigma_\eta} E^H E + \Sigma_m^{-1} \right]^{-1} \frac{1}{\sigma_\eta} E^H (\mathbf{y} - E\mu_m), \end{aligned}$$

where the mean and covariance values for the priors can be obtained from a low resolution image of the same object. A similar idea has been applied in k-t SENSE and k-t PCA methods in the dynamic imaging setting to exploit spatio-temporal correlations [22, 10].

Simultaneous use of different priors has also been suggested for dynamic imaging. Some authors used a sparse-low rank decomposition with separate regularizers for the sparse and low rank part of dynamic images, using the Schatten-p norm for the rank norm [8].

In this work, we propose to use a prior term that is learned from example images in an unsupervised way. In particular, we approximate  $-\log p(\mathbf{m})$  with a neural network model using a dataset of fully sampled images. We train a VAE on patches of fully sampled MR images to capture the distribution of patches using a parametric latent model and use this prior for reconstruction.

---

<sup>2</sup>Where we used the change of variables rule to relate the distributions [21].

## 2.2 Learning the data distribution with VAEs

VAE is an unsupervised learning algorithm used to approximate high-dimensional data distributions [17, 18]. In computer vision, these models have been used to approximate distribution of natural images and generate samples from them. In this section, we provide a brief overview of the VAE algorithm. We keep our description very generic and only link it to MR image data at the end.

The main goal of the VAE algorithm is to approximate the data distribution using a latent model given as

$$p(\mathbf{x}) = \int_{\mathbf{z}} p(\mathbf{x}, \mathbf{z}) d\mathbf{z} = \int_{\mathbf{z}} p(\mathbf{x}|\mathbf{z}) p(\mathbf{z}) d\mathbf{z}, \quad (10)$$

where  $\mathbf{z} \in \mathbb{R}^L$  denote the latent variables,  $\mathbf{x} \in \mathbb{R}^P$  the data and  $p(\mathbf{z})$  the prior over the  $\mathbf{z}$ 's. Direct computation of  $p(\mathbf{x})$ ,  $\log(p(\mathbf{x}))$  or  $p(\mathbf{z}|\mathbf{x})$  requires integrating over  $\mathbf{z}$ , which is not feasible even with relatively small  $L$ . Variational approximation uses an approximate distribution for the posterior  $q(\mathbf{z}|\mathbf{x}) \approx p(\mathbf{z}|\mathbf{x})$  to address this problem. Using the approximation,  $\log p(\mathbf{x})$  can be decomposed into two terms [24]

$$\log p(x) = \text{ELBO} + \text{KLD} = \mathbb{E}_{q(\mathbf{z}|\mathbf{x})} \left[ \log \frac{p(\mathbf{x}, \mathbf{z})}{q(\mathbf{z}|\mathbf{x})} \right] + \text{KL} [q(\mathbf{z}|\mathbf{x}) || p(\mathbf{z}|\mathbf{x})]. \quad (11)$$

The first term is referred to as the evidence lower bound (ELBO) and the second term is the Kullback-Leibler divergence (KLD) between the approximate and true posterior. ELBO can further be decomposed into two terms as

$$\begin{aligned} \text{ELBO} &= \mathbb{E}_{q(\mathbf{z}|\mathbf{x})} \left[ \log p(\mathbf{x}|\mathbf{z}) + \log \frac{p(\mathbf{z})}{q(\mathbf{z}|\mathbf{x})} \right] \\ &= \mathbb{E}_{q(\mathbf{z}|\mathbf{x})} [\log p(\mathbf{x}|\mathbf{z})] - \text{KL} [q(\mathbf{z}|\mathbf{x}) || p(\mathbf{z})] \end{aligned} \quad (12)$$

$$= \log p(\mathbf{x}) - \text{KL} [q(\mathbf{z}|\mathbf{x}) || p(\mathbf{z}|\mathbf{x})], \quad (13)$$

where the last equality is simply a reformulation of Equation 11. The first term in Equation 12 is the expectation of the posterior of  $\mathbf{x}$ 's with respect to the approximate posterior of the  $\mathbf{z}$ 's which we refer to as the data likelihood. The second term measures the divergence between the approximate distribution and the prescribed prior distribution  $p(\mathbf{z})$ .

We see from Equation 13 that ELBO is a lower bound for  $\log p(x)$  since KLD is always larger than 0. As in any variational inference approach, VAE parameterizes the data likelihood and the approximate posterior, i.e.  $q(\mathbf{z}|\mathbf{x}) = q_\theta(\mathbf{z}|\mathbf{x})$  and  $p(\mathbf{x}|\mathbf{z}) = p_\phi(\mathbf{x}|\mathbf{z})$ , and maximize ELBO for a given set of data samples with respect to  $\theta$  and  $\phi$ . Maximizing ELBO will minimize the KLD and maximize  $\log p(\mathbf{x})$ . The underlying assumption here is that if  $q_\theta(\mathbf{z}|\mathbf{x})$  is a powerful approximation, i.e. if  $p(\mathbf{z}|\mathbf{x})$  lives in the space of functions, which  $q_\theta(\mathbf{z}|\mathbf{x})$  can approximate, then the KLD term in Equation 11 will be close to zero for optimal  $\theta$ , which means ELBO with the optimal parameters will be a good approximation to  $\log p(\mathbf{x})$ .

The VAE algorithm uses neural networks to parameterize both  $q_\theta(\mathbf{z}|\mathbf{x})$  and  $p_\phi(\mathbf{x}|\mathbf{z})$ , where  $\theta$  and  $\phi$  are the parameters of the corresponding networks. The networks  $q_\theta(\mathbf{z}|\mathbf{x})$  and  $p_\phi(\mathbf{x}|\mathbf{z})$  are called the encoder and the decoder, respectively. The former takes the data sample  $\mathbf{x}$  and encodes it into a posterior distribution in the latent space with network parameters  $\theta$ . If the posterior distribution is modelled as a Gaussian, then the encoder outputs a mean and a covariance matrix for  $\mathbf{z}$  depending on  $\mathbf{x}$ . This is in contrast to a regular autoencoder, where encoder would map  $\mathbf{x}$  to a specific  $\mathbf{z}$  in a deterministic fashion. The decoder network on the other hand, takes a latent vector  $\mathbf{z}$  and maps it to a conditional distribution of the data given  $\mathbf{z}$  with the network parameterized by  $\phi$ .

In the training phase,  $\phi$  and  $\theta$  are optimized to maximize the ELBO

$$\max_{\theta, \phi} \mathbb{E}_{\mathbf{x} \sim p(\text{data})} [\text{ELBO}(\mathbf{x}, \theta, \phi)] \approx \max_{\theta, \phi} \frac{1}{N} \sum_{n=1}^N \mathbb{E}_{q_\theta(\mathbf{z}|\mathbf{x}^n)} [\log p_\phi(\mathbf{x}^n|\mathbf{z})] - \text{KL} [q_\theta(\mathbf{z}|\mathbf{x}^n) || p(\mathbf{z})], \quad (14)$$

where  $\mathbf{x}^n$  is the  $n^{th}$  training sample. During this optimization the KL term forces the posterior of  $\mathbf{z}$  to remain close to the prior distribution  $p(\mathbf{z})$  for all examples. The data likelihood term on the other hand, forces the model to faithfully reconstruct observed samples from the latent space. After the training, we can sample from the  $p(\mathbf{x})$  approximation by simply sampling a  $\mathbf{z}$  vector from the prior distribution and feeding this into the decoder to generate a new data sample.

Practical implementation of the VAEs require several design choices. In this work, we use the vanilla VAE [17] except for the data likelihood. We use an isotropic unit Gaussian for the prior term,  $p(\mathbf{z}) = N(0, \mathbf{I})$ . For the data likelihood term, we use a multi-modal Gaussian  $p_\phi(\mathbf{x}|\mathbf{z}) = N(\mathbf{x}|\boldsymbol{\mu}_\phi(\mathbf{z}), \boldsymbol{\Sigma}_\phi(\mathbf{z}))$ , different from the vanilla implementation, similar to [25]. The approximate distribution  $q(\mathbf{z}|\mathbf{x})$  is given as  $N(\mathbf{z}|\boldsymbol{\mu}_\theta(\mathbf{x}), \boldsymbol{\Sigma}_\theta(\mathbf{x}))$ . Lastly, we use diagonal covariance matrices for both  $\boldsymbol{\Sigma}_\phi(\mathbf{z})$  and  $\boldsymbol{\Sigma}_\theta(\mathbf{x})$ .

The expectations in the optimization problem in Equation 14 are estimated by sampling and the entire model is optimized by back-propagation. First, for each sample  $\mathbf{x}^n$ ,  $\boldsymbol{\mu}_\theta(\mathbf{x}^n)$  and  $\boldsymbol{\Sigma}_\theta(\mathbf{x}^n)$  are computed and a  $\mathbf{z}^n$  is sampled. With the sampled  $\mathbf{z}^n$ ,  $\boldsymbol{\mu}_\phi(\mathbf{z}^n)$  and  $\boldsymbol{\Sigma}_\phi(\mathbf{z}^n)$  are computed and the data likelihood term is evaluated. For the gradients to be able to flow through the random variable  $\mathbf{z}$ , a reparameterization trick is used in the VAE algorithm to sample  $\mathbf{z}^n$ . Instead of sampling directly from the posterior, a random variable  $\epsilon$  is sampled, where  $\epsilon \propto N(0, \mathbf{I})$  and the latent variable is constructed using  $\mathbf{z}^n = \boldsymbol{\mu}_\theta(\mathbf{x}^n) + \epsilon \boldsymbol{\Sigma}_\theta^{1/2}$ . We refer the reader to [17] for further details.

In our model, we use the VAE model to approximate the prior distribution of magnitude of 2D MR patches of fully sampled images. We approximate  $p(|\mathbf{x}|)$ , where  $\mathbf{x}$  is a patch extracted from a complex valued MR image of size  $\sqrt{P}\mathbf{x}\sqrt{P}$ . In order to train the VAE model, we use patches extracted from existing fully sampled images. We use multi-layer convolutional neural networks for both the encoder and the decoder. Both networks have small kernels of stride one in the convolutions and no pooling to avoid loss of spatial resolution. We provide the exact parameters of the network design in Section 2.5 and continue with the description of the proposed model in the next part.

### 2.3 Reconstruction model with the learned prior

Once the network is trained and optimal values  $\theta^*$  and  $\phi^*$  are found, we can integrate the prior within a Bayesian formulation of the reconstruction problem. We make two key observations to achieve this. First, an approximate log likelihood of an image patch  $\mathbf{x}$  can be obtained by evaluating  $\text{ELBO}(|\mathbf{x}|)$  with the optimal parameters.

$$\text{ELBO}(|\mathbf{x}|) = \mathbb{E}_{q_{\theta^*}(\mathbf{z}||\mathbf{x}|)} \left[ \log p_{\phi^*}(|\mathbf{x}||\mathbf{z}) + \log \frac{p(\mathbf{z})}{q_{\theta^*}(\mathbf{z}||\mathbf{x}|)} \right], \quad (15)$$

where we use the magnitude of the patch  $|\mathbf{x}|$  within the ELBO. Using the ELBO of the image patches and dropping out the subscripts denoting the optimal parameters for the sake of simpler notation, we formulate the proposed model as the following MAP estimation problem

$$\arg \min_{\mathbf{m}} \|E\mathbf{m} - \mathbf{y}\|_2^2 - \sum_{r \in \Omega(\mathbf{m})} \text{ELBO}(|\mathbf{x}_r|), \quad (16)$$

where  $\Omega(\mathbf{m})$  denotes a set of (overlapping) patches covering the image  $\mathbf{m}$  and the summation goes over all the patches and  $|\mathbf{x}_r|$  is the magnitude of the  $r^{th}$  image patch. Note that we assume independence between different patches. This approach ignores statistical dependencies between different patches of the same image however, makes the computations much easier.

The problem given in Equation 16 cannot be solved directly since an exact computation of the ELBO term requires evaluating the expectation with respect to  $q(\mathbf{z}||\mathbf{x}|)$ , which is computationally not feasible. Instead, we use a Monte Carlo sampling approach to calculate the ELBO as follows

$$\text{ELBO}(|\mathbf{x}|) \approx \frac{1}{J} \sum_{j=1}^J \log p(|\mathbf{x}||\mathbf{z}^j) + \log \frac{p(\mathbf{z}^j)}{q(\mathbf{z}^j||\mathbf{x}|)}, \text{ with } \mathbf{z}^j \sim q(\mathbf{z}||\mathbf{x}|). \quad (17)$$

Here  $J$  represents the number of Monte-Carlo samples.

Another key observation is that the approximation in Equation 17 is differentiable since each term is defined through networks that are themselves differentiable. This is the critical aspect that allows integrating the trained VAE as a prior into an optimization based reconstruction algorithm. Plugging the ELBO approximation into Equation 16, we obtain the formulation of the reconstruction problem

$$\arg \min_{\mathbf{m}} \|E\mathbf{m} - \mathbf{y}\|_2^2 - \sum_{r \in \Omega(\mathbf{m})} \left[ \frac{1}{J} \sum_{j=1}^J \log p(|\mathbf{x}_r| | \mathbf{z}^j) + \log \frac{p(\mathbf{z}^j)}{q(\mathbf{z}^j | |\mathbf{x}_r|)} \right], \text{ where } \mathbf{z}^j \sim q(\mathbf{z} | |\mathbf{x}_r|), \quad (18)$$

where the first term is the usual data term and the second term within the summation is the regularization term that arises from the learned prior.

We can compute the total derivative of the prior term with respect to each image patch as follows

$$\mathcal{R}(|\mathbf{x}|, \mathbf{z}^j) \triangleq \log p(|\mathbf{x}| | \mathbf{z}^j) + \log \frac{p(\mathbf{z}^j)}{q(\mathbf{z}^j | |\mathbf{x}|)} \quad (19)$$

$$\frac{d}{d\mathbf{x}} \left[ \frac{1}{J} \sum_{j=1}^J \mathcal{R}(|\mathbf{x}|, \mathbf{z}^j) \right] = \frac{1}{J} \sum_{j=1}^J \frac{d}{d\mathbf{x}} \mathcal{R}(|\mathbf{x}|, \mathbf{z}^j) \quad (20)$$

$$= \frac{\mathbf{x}}{|\mathbf{x}|} \left[ \frac{1}{J} \sum_{j=1}^J \frac{\partial}{\partial |\mathbf{x}|} \mathcal{R}(|\mathbf{x}|, \mathbf{z}^j) + \frac{\partial}{\partial \mathbf{z}^j} \mathcal{R}(|\mathbf{x}|, \mathbf{z}^j) \frac{d\mathbf{z}^j}{d|\mathbf{x}|} \right], \quad (21)$$

where we defined  $\mathcal{R}(\mathbf{x}, \mathbf{z}^j)$  for notational simplicity. The second term in the last line is due to the dependency of the samples  $\mathbf{z}^j$  to  $\mathbf{x}$ . The term  $\mathbf{x}/|\mathbf{x}|$  is due to taking the derivative of the magnitude with respect to the image patch. There are two points to note here. First, the derivative operators are inside the summation with respect to  $j$ , which corresponds to finding the partial derivative of different samples separately and taking their average. This operation can therefore be implemented in parallel both for different patches as well as different Monte-Carlo samples. We implement the derivative of the prior term using automatic symbolic differentiation in Tensorflow [26]. When evaluating derivatives of the patches, we feed a batch of size  $W \cdot S$  containing all the patches and multiple copies of each patch. By doing this we can evaluate the derivatives for all  $W$  patches in one go and also evaluate  $S$  Monte Carlo samples for each of them, which we can average afterwards. By doing so we avoid a time consuming for-loop, that would be otherwise necessary to loop over the Monte Carlo samples. Second, the derivative in Equation 21 will have the same phase as the patch  $\mathbf{x}$  because the term within the brackets is real therefore, the only phase is coming from  $\mathbf{x}$  itself.

## 2.4 Optimization using projection onto convex sets

We solve the optimization problem given in Equation 18 using the projection onto convex sets (POCS) algorithm [27], specifically using the formulation in [28]. POCS is an iterative minimization process, where the solution variable is projected onto convex sets, each defined by one of the constraints in the problem.

The projection for the data consistency term is given simply as  $\mathcal{P}_{DC}\mathbf{m} = \mathbf{m} - E^H(E\mathbf{m} - \mathbf{y})$  [27]. Since we do not have a projection operator for the prior term, we approximate it by several gradient ascent steps with a small step size. We use the final image patch at the end of the ascent steps as the projected image patch.

We denote the projection of  $\mathbf{x}$  with respect to the prior term with  $\mathcal{P}_{prior}\mathbf{x} = \mathbf{x}^K$  where we define  $\mathbf{x}^K$  as the result of  $K$  gradient ascent steps each being

$$\mathbf{x}^{k+1} = \mathbf{x}^k + \alpha \left[ \frac{\mathbf{x}}{|\mathbf{x}|} \left\{ \frac{1}{J} \sum_{j=1}^J \frac{\partial}{\partial |\mathbf{x}|} \mathcal{R}(|\mathbf{x}|, \mathbf{z}_j) + \frac{\partial}{\partial \mathbf{z}_j} \mathcal{R}(|\mathbf{x}|, \mathbf{z}_j) \frac{d\mathbf{z}_j}{d|\mathbf{x}|} \right\} \right]_{\mathbf{x}=\mathbf{x}^k} \quad (22)$$

---

**Algorithm 1** VAE reconstruction using POCS. See text for a more detailed explanation.

---

```

1:  $y$ : undersampled k-space data
2:  $E$ : undersampling encoding operator
3: VAE: the trained VAE
4: procedure VARECON( $y, E, \text{VAE}$ )
5:    $\mathbf{m}^0 \leftarrow E^H y$  ▷ initialize with the undersampled image
6:   for  $t = 0 : T - 1$  do ▷ POCS iterations
7:      $\{\mathbf{x}_r^t\} \leftarrow \text{image2patches}(\mathbf{m}^t)$  ▷ creates a set of patches covering the image
8:     for  $k = 0 : K - 1$  do ▷ iterations for the prior projection  $\mathcal{P}_{prior}$ 
9:       for  $r = 1 : \text{no of patches}$  do ▷ loop over all the patches in  $\{\mathbf{x}_r^t\}$ 
10:         $\mathbf{x}_r^{k+1} \leftarrow \mathbf{x}_r^k + \alpha \left[ \frac{\mathbf{x}}{|\mathbf{x}|} \left\{ \frac{1}{J} \sum_{j=1}^J \frac{\partial}{\partial |\mathbf{x}|} \mathcal{R}(|\mathbf{x}_r|, \mathbf{z}_j) + \frac{\partial}{\partial \mathbf{z}_j} \mathcal{R}(|\mathbf{x}_r|, \mathbf{z}_j) \frac{d\mathbf{z}_j}{d|\mathbf{x}|} \right\} \right]_{\mathbf{x}=\mathbf{x}^k}$  ▷ update
        patches acc. to Eq. 22
11:       end for
12:     end for
13:      $\mathbf{m}^t \leftarrow \text{patches2image}(\{\mathbf{x}_r^K\})$  ▷  $\mathcal{P}_{prior} \mathbf{m}^t$ 
14:      $\mathbf{m}^t \leftarrow |\mathbf{m}^t|$  ▷  $\mathcal{P}_{abs} \mathbf{m}^t$ 
15:      $\mathbf{m}^{t+1} \leftarrow \mathbf{m}^t - E^H (E \mathbf{m}^t - y)$  ▷  $\mathcal{P}_{DC} \mathbf{m}^t$ 
16:   end for
17:   return  $\mathbf{m}^T$  ▷ Resulting reconstruction
18: end procedure

```

---

scaled with the step size  $\alpha$ . We apply the gradient ascent steps for each patch independent from the others. To reduce edge effects resulting from patchwise projections, we use two sets of overlapping patches and average the derivatives where they overlap.

As the likelihood term is only trained on magnitude images and cannot convey any information regarding the phase of the image, we also use a phase projection following the prior projection, where we set the phase of the patch to zero, given as  $\mathcal{P}_{abs} \mathbf{x} = |\mathbf{x}|$ . Notice we can do this because we expect the images being reconstructed to have zero phase in this specific application. It is however possible to change this to any other constraint on the phase of the image, such as a low resolution estimation of the phase [3] or zero-divergence constraint for phase contrast flow imaging reconstruction [29].

With the data consistency, prior and phase projections defined as above, one step of reconstruction within the POCS framework becomes

$$\mathbf{m}^{t+1} = \mathcal{P}_{DC} \mathcal{P}_{abs} \mathcal{P}_{prior} \mathbf{m}^t. \quad (23)$$

We apply  $T$  POCS steps to complete the reconstruction. Algorithm 1 provides a summary of the reconstruction procedure.

## 2.5 Details on VAE network architecture and training

In our implementation we use a patch size of 28x28. For both the encoding,  $q_\theta(\mathbf{x}|\mathbf{z})$ , and decoding  $p_\phi(\mathbf{z}|\mathbf{x})$ , we use convolutional networks combined with fully connected layers and we use 60 dimensional latent variables. Both networks are depicted in Figure 1. For the encoding network, the input is an image patch and the output is mean and covariance matrix of the latent variables. We implement three convolutional layers with 32, 64 and 64 channels, respectively. We use stride of 1, no pooling and each convolutional layer has a ReLU activation. Output of the last convolutional layer is reshaped and connected to two fully connected layers with connection matrices 64\*784x60. The fully connected layers generate two vectors of size 60, the mean  $\mu_\theta(\mathbf{x})$  and covariance  $\Sigma_\theta(\mathbf{x})$  of the approximate posterior  $q(\mathbf{z}|\mathbf{x})$ .



The decoding network starts with a fully connected layer with the weight matrix  $60 \times 784 \times 48$ . Output is reshaped and fed into three convolutional layers with 48, 90 and 90 channels, respectively. As in the encoding network, we use stride of 1, no pooling and each layer has a ReLU activation. Output of the third convolutional layer is connected to two convolutional layers with a single channel each. No non-linear activation function is used here. Outputs of these last layers are the mean,  $\mu_\phi(\mathbf{z})$ , and variance maps,  $\Sigma_\phi(\mathbf{z})$ . All convolutional layers for both decoding and encoding networks use  $3 \times 3$  kernels and all layers also have additive bias terms throughout the network.

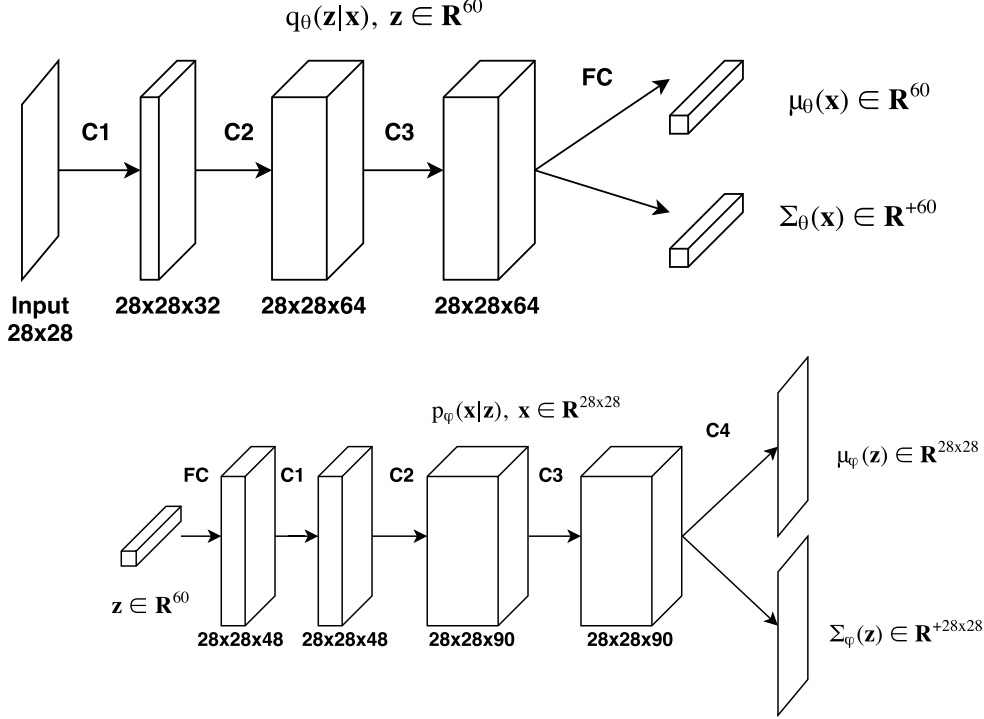


Figure 1: Architecture of the encoding (top) and decoding (bottom) networks of our VAE. Arrows indicated with  $C\#$  are convolutional layers followed by ReLU non-linear activation except  $C4$  of decoding network, which is not followed by non-linear activation. Arrows indicated by FC are fully connected layers. FC of the decoding network is followed by a ReLU activation but not of the encoding network.

We use a batch size of 50 for training the VAE network. Due to stability issues we use the log of the variance values throughout the network. Taking the exponential ensures the variance values are always positive. We initialize the network weights with a truncated normal initializer with standard deviation 0.05. We use Adam [30] to optimize the loss function with a learning rate of  $5e-4$  and default momentum values in Tensorflow.

### 3 Experimental setup

In this section, we provide details on our experimental setup, including data and evaluation strategy. In the following section, we present results.

### 3.1 MR image data

We evaluated our method using structural images from the Human Connectome Project (HCP)<sup>3</sup> data set [31]. This choice was motivated by the fact that the high quality of HCP images are ideal for learning priors and there is a large number of images for training the VAE model.

We took 2D slices from the T1 weighted 3D MPRAGE images acquired with parameters 2400 ms, 2.14 ms and 1000 ms for TR, TE and TI, respectively, flip angle of 8 degrees, a standard field of view for all subjects of 224x224x224 mm<sup>3</sup> with 0.7 mm isotropic resolution using a bandwidth of 210 Hz/voxel. Images were acquired with a 3T Siemens device. Fat suppression was used during acquisition. In our experiments, we used the minimally preprocessed images in order to also have the corresponding FreeSurfer [32] segmentations, which we use in our evaluation. Images were resampled to 1mm isotropic resolution with FOV matrix 260x311x260 and were rigidly aligned. Despite the rigid alignment, there were substantial local orientation differences in the images from different subjects. For our experiments, we used five central slices with skipping four slices between each. We cropped the images to a size of 252x308, which is a multiple of our patch size, reducing the computational load. We normalized the images by mapping their 95<sup>th</sup> percentile to 1.

In the experiments, we selected images from 158 subjects as training data and used them to train the prior VAE model. Our training set comprises of 790 slices extracted from 158 different subjects, 5 slices from each. We trained the VAE on image patches of size 28x28. For each batch, we randomly sampled 50 patches from the training images. We did not generate fixed patch positions but rather sampled patches from random locations. We trained the VAE model for 200k iterations. We selected 10 central slices from 10 subjects from the HCP data set as test data and present reconstruction results on these images. Subjects used in training and test sets were separated.

As an additional experiment, to test if the proposed reconstruction method can be used on a domain that is different from the one the prior is trained on, we experimented with two 2D slices from the Alzheimer’s Disease Neuroimaging Initiative (ADNI) data set. The ADNI images were selected from subjects with Alzheimer’s disease and who have visible white matter lesions. Our subgoal in this selection was to also test whether the proposed method will be able to faithfully reconstruct lesions. The acquisition parameters of the ADNI data set were different than HCP: TR, TE, TI values are 7.34 ms, 3.03 ms, 400 ms, flip angle is 11 degrees, FOV matrix 196x256x256 with resolution 1.2 mm x 1 mm x 1 mm. Images were acquired with a 3T GE scanner with no fat suppression. Images were bias-field corrected with the N3 algorithm [33]. We used a central slice from each subject where the white matter lesions were visible. For these images, FOV matrix was 196x224 and the resolution was 1.2 mm x 1 mm. We further cropped the FOV to 168x224 to get rid of the empty regions in the image to accelerate computations. We normalized the images the same way as the HCP data.

### 3.2 Setup and evaluation

In our assessment, we artificially undersampled the images of the test subjects in k-space and reconstructed them back. We experimented with varying undersampling ratios, which we denote with  $R$  when presenting results.

We use Cartesian undersampling in one dimension while fully sampling in the other dimension, corresponding to phase-encoding and readout directions, respectively. We show some examples of these patterns in Figures 3 and 4. We generated the patterns by randomly sampling a 1D Gaussian distribution along the phase-encoding dimension with denser sampling at the center of the k-space. We randomly drew many sampling patterns from the Gaussian distribution and selected the ones with the best peak-to-side ratio. In addition, we added the central 15 profiles to these selected patterns

---

<sup>3</sup>Further details of the HCP data set can be found in HCP-S500+MEG2-Release-Reference-Manual and HCP-S1200-Release-Appendix-I (obtainable from <https://www.humanconnectome.org/study/hcp-young-adult/document/500-subjects-data-release>)

to fully sample the low-frequency components. We used 2 and 3 for undersampling ratios and used appropriate Gaussians to generate the sampling patterns. The net undersampling factor is computed as the total number of profiles divided by the number of sampled profiles, including the central 15 ones that are added. We assumed a single coil imaging with uniform sensitivity throughout the experiments for the proof of concept, however the proposed method works independent of the number of coils.

While assessing VAE, we generated a new undersampling pattern for each test image to make sure the reconstruction results covered the variability of the undersampling patterns. We reconstructed the images using 30 POCS iterations ( $T=30$ ), 10 iterations for the prior projection ( $K=10$ ) and the step size  $\alpha=1e-4$  as defined in section 2.4 and Algorithm 1.

We quantitatively evaluated the proposed method by comparing the reconstructions with the fully sampled “ground truth” images. We used Root-Mean-Squared-Error (RMSE) between reconstruction and ground truth, Contrast-to-Noise-Ratio (CNR) and Contrast difference (CN) computed at the gray and white matter boundary in the brain. In order to obtain white matter boundaries we applied binary erosion (with a square structuring element of size  $7 \times 7$ ) to the white matter segmentations and took the difference of the original and eroded segmentations. This provided us a band around the boundary that we used to compute CNR and CN. We computed the mean and standard deviations of these metrics across the test samples and provide these statistics.

### 3.3 Compared methods

As a basic benchmark, we evaluated zero-filling reconstructions, which are simply an inverse encoding operation applied on the k-space. In addition we used three alternative methods. As the first baseline, we used total variation (TV) reconstruction as described in [3]. We used the BART toolbox implementation that is publicly available [34]. We used the “pics” tool with TV regularization (regularization strength 0.075) and the ADMM parameter  $\rho$  as 1. We used 20 conjugate gradient steps and 4500 total iterations (full command is “bart pics -R T:3:0:0.0075 -u1 -C20 -i4500”).

As the second method, we used reconstruction using dictionary learning (DL) [35], where the implementation is available online<sup>4</sup>. We used 200 iterations, a patch size of 36 voxels and 36 dictionary atoms. Furthermore, we set number of signals used for training to 7200 and the overlap stride to 2. We used K-SVD learning with both sparsity and error threshold. The sparsity level was set to 7. The error threshold was set to 0.046 for the first four iterations, then to 0.0322 for the rest of the iterations. We used 15 K-SVD iterations. These settings are based on the original article and the code provided.

Lastly, we used the recently proposed ADMM-Net [16], for which the code is provided online<sup>5</sup> by the authors. We modified the code very slightly to work with non-square images and Cartesian undersampling patterns. To train the model, we used the same 790 images, which we used to train the VAE model. ADMM-Net training requires both undersampled and fully-sampled versions of the training images. Furthermore, it requires the undersampling pattern to be fixed. To train the ADMM-Net, we fixed the undersampling pattern, both for  $R=2$  and 3, throughout the training for all images. At test time we used the same undersampling patterns. We used 15 stages with 8 filters (filter size  $3 \times 3$ ), padding as 1. We did not use weight decay during training. We set the maximum iteration number to 25 for the L-BFGS algorithm. It trained to maximum iterations for  $R=2$  (45 hours) and 13 iterations before convergence for  $R=3$  (42 hours) on a GPU (GeForce GTX TITAN X). The normalized mean squared errors were 0.078 and 0.035 before and after training for  $R=2$  and 0.11 and 0.071 for  $R=3$ . We tried to optimize the settings to achieve the best possible results with the HCP data.

<sup>4</sup>Code available at <http://www.ifp.illinois.edu/~yoram/DLMRI-Lab/Documentation.html>

<sup>5</sup><https://github.com/yangyan92/Deep-ADMM-Net>

## 4 Results

### 4.1 Image patches sampled from the learned prior

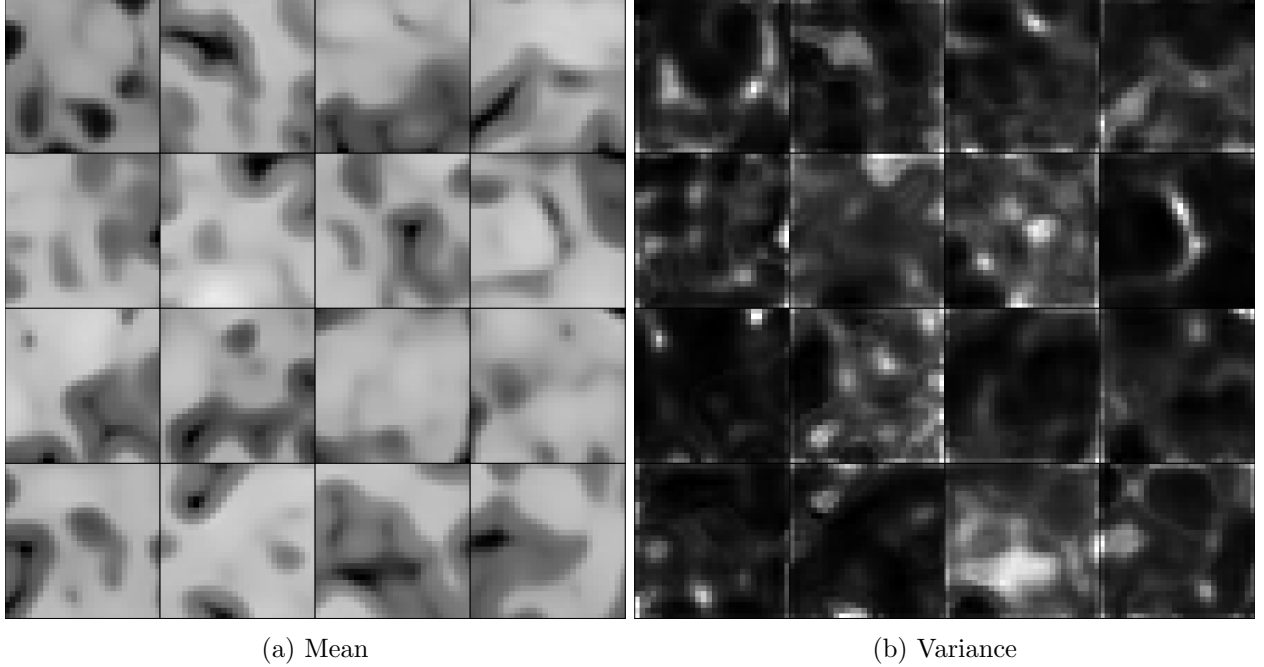


Figure 2: 16 image patches sampled from the prior learned by the VAE algorithm. Images on the left are the mean predictions and the images on the right are the corresponding variance maps. The patches are 28x28 and the VAE model was trained with images from the HCP data set.

We start by showing patches sampled from the prior model in Figure 2. We sampled 16 image patches of size 28x28 from the trained VAE prior model. These patches were generated by simply feeding 16 random  $\mathbf{z}$  vectors drawn from unit Gaussian to the decoder network. The decoder network outputs a mean image, i.e.  $\mu_\phi(\mathbf{z})$ , and a corresponding variance image, i.e.  $\Sigma_\phi(\mathbf{z})$ . Mean image patches are shown on the left and the corresponding variance images on the right. We would like to note that we have not cherry-picked these images and took the images generated with the first 16 random  $\mathbf{z}$  vectors. The sampled patches look realistic where gray matter, white matter and gyri/sulci structures are clearly defined. Notice that the network learns on its own to put gray matter between white matter and cerebrospinal fluid (CSF). These generated samples suggest that the VAE algorithm is able to learn the underlying distribution of MR patches. The images on the right show that VAE places high variance in the CSF areas as well as boundaries between structures. We observe that isolated gray matter or CSF islands receive high variance.

### 4.2 Reconstructions - visual results

Next, we show visual reconstruction results for the proposed method and the competing methods. Figure 3 shows a test image from the HCP data set, its undersampled version and the reconstruction results for undersampling ratio  $R=2$ . The sampling pattern is also shown in the figure. We observe that the skull results in quite prominent aliasing artifacts due to its relatively high intensity even with this low undersampling ratio. All the methods achieve good reconstruction quality in terms of reproducing structural information. The small triangle shaped gray matter structure shown in the zoomed fully-sampled image, is faithfully reconstructed by all the methods. Total variation results in a

cartoon-like image, as expected. All other methods retain the texture information. VAE and DLMRI reconstructions are sharper while ADMM-Net result has some blurring effect. The error images show higher error in regions where gray matter and white matter structures are intertwined.

Aliasing artifacts become more prominent at  $R=3$  as seen in Figure 4. At this ratio the TV reconstruction is not satisfactory, aliasing artifacts are not completely removed. ADMM-Net reconstruction performs well in de-aliasing, however the output image is blurry, contrast between gray and white matter is compromised and gyri/sulci structures are not well-defined. DLMRI performs better than TV and ADMM-Net, however, it also loses some contrast and blurs gray-white matter boundaries. Our proposed VAE reconstructs the image without blurring and losing contrast between gray and white matter. Observing the zoomed images, we note that the triangle shaped gray matter island is nearly lost in all reconstructions except for VAE. All other methods hint at a structure, however not in a clearly visible fashion. The VAE reconstruction maintains contrast in the area and although it loses some details, it can reconstruct the gray matter structure fairly faithfully. Overall the proposed VAE method retains the texture, structural and contrast information the best compared to the alternatives. Undersampling and reconstruction results shown in both figures are produced with the undersampling pattern that was used to train the ADMM-Net for comparability.

We also show four more randomly selected images from the test set in supplementary Figures S2 and S3. In these figures, the undersampling pattern is the different for each image, however same among the methods for a given image. Additionally a plot showing convergence of the POCS algorithm can be seen in Figure S1.

### 4.3 Reconstructions - quantitative results

We present the quantitative results for reconstruction accuracy in Table 1. The table reports means and standard deviations in parentheses for different quality metrics obtained from  $N=10$  test images. We note again that the test subjects are separate from the training subjects used to train VAE and ADMM-Net models and each of the images are from different subjects.

To assess statistical significance of differences in accuracy measures, we used Wilcoxon signed rank test, a paired and non-parametric method, and used  $p=0.05$  threshold. Here we used the same undersampling pattern for all methods except for ADMM-Net and changed the pattern for each test image. ADMM-Net reconstructed all images with the same undersampling pattern that was used in training, following the original implementation of the authors. Due to this limitation, we refrain from doing a pairwise test between the proposed method and ADMM-Net.

The VAE reconstruction outperforms all the other methods in all cases. TV outperforms DLMRI for  $R=2$  in terms of RMSE, which is a result of denoising rather than better quality reconstruction as DLMRI results are visually more realistic than TV.

### 4.4 Reconstruction - ADNI examples

Lastly, we show VAE reconstructions in Figure 5 for the images of two Alzheimer’s disease (AD) patients from the ADNI data set with white matter lesions for  $R=2$ . We used the VAE model trained on HCP images, which is composed of healthy subjects, to reconstruct the AD examples here. The reconstructed images recover gray matter-white matter structures and edges faithfully. The white matter lesions are also well reconstructed. The error maps show similar behavior to HCP reconstructions and do not indicate a specific increase of error in the lesion regions.

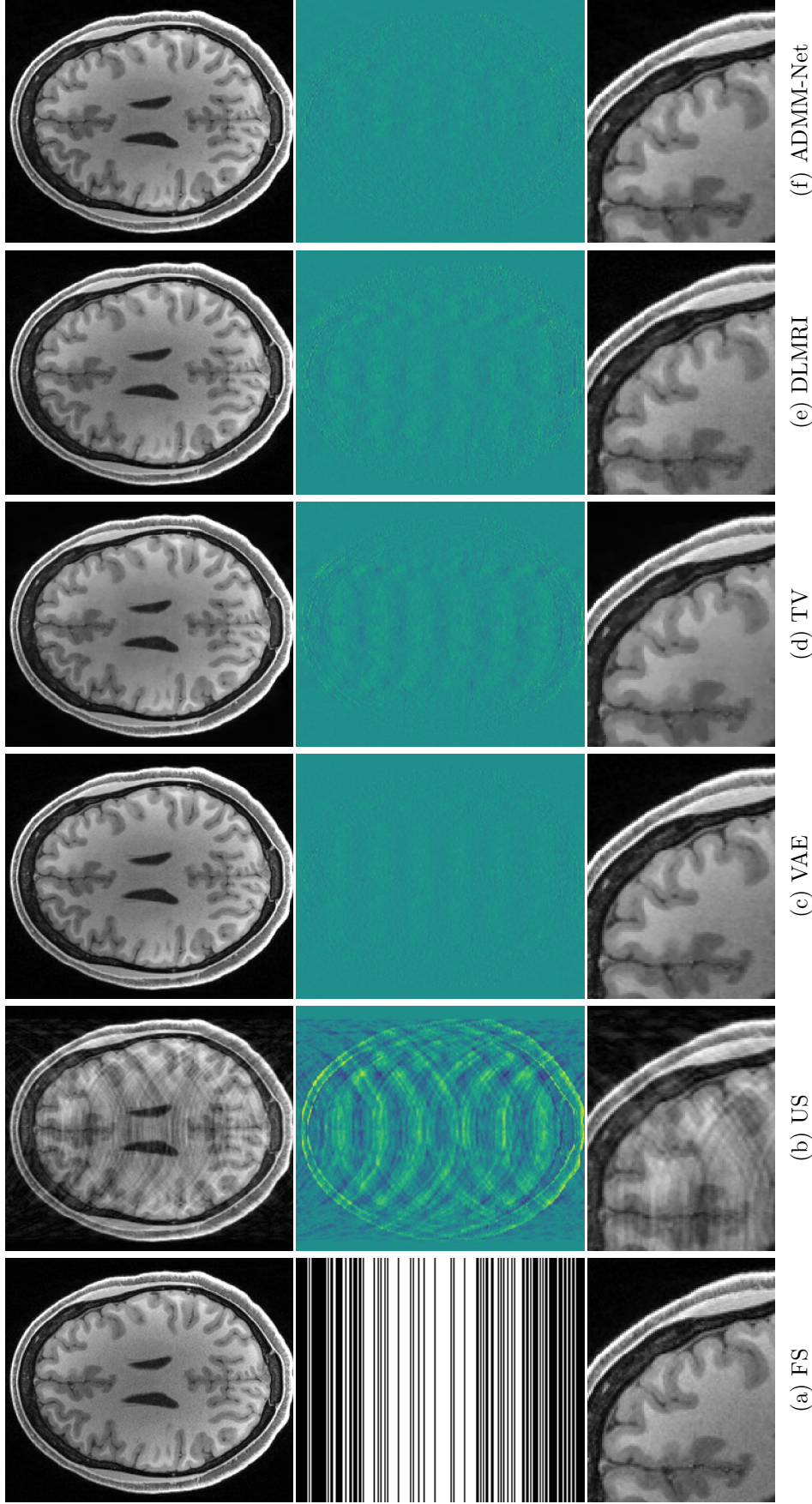


Figure 3: Reconstruction results for  $R=2$ . First row shows the fully sampled image (FS), the undersampled image (US) and the results of different reconstruction methods. Second row shows the used undersampling pattern and the error maps (intensities clipped to  $(-0.3, 0.3)$ ). Third row shows a zoomed in part of the images.



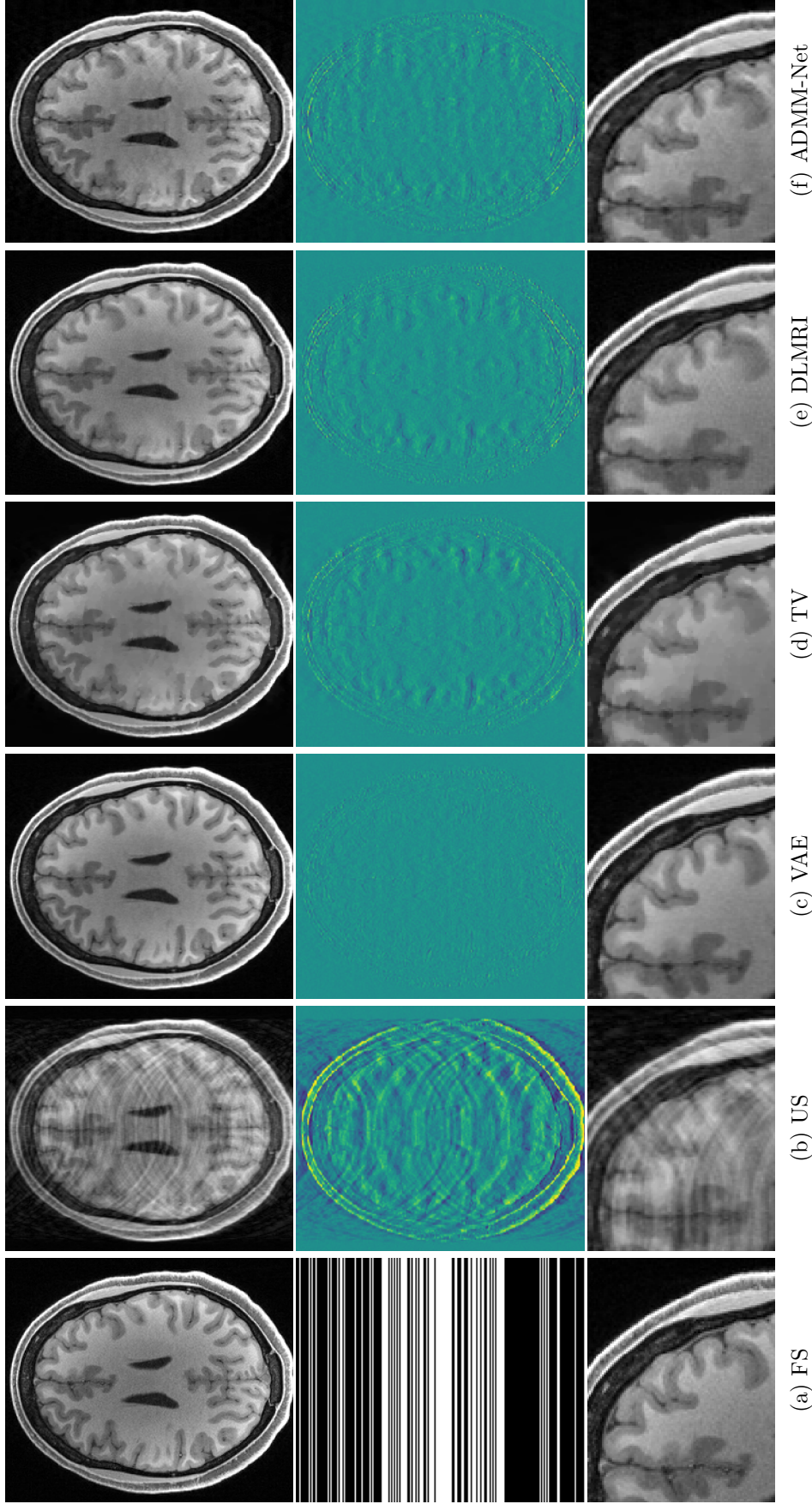


Figure 4: Reconstruction results for  $R=3$ . First row shows the fully sampled image (FS), the undersampled image (US) and the results of different reconstruction methods. Second row shows the used undersampling pattern and the error maps (intensities clipped to  $(-0.3, 0.3)$ ). Third row shows a zoomed in part of the images.

## 5 Discussion

In this paper we proposed a novel method for MR reconstruction from undersampled k-space acquisitions. The method uses the VAE algorithm to learn the distribution of MR patches from a training set composed of fully sampled images. The model then uses this learned distribution as a probabilistic prior in a Bayesian reconstruction framework. We showed experimentally that the proposed method outperforms three widely used MR reconstruction techniques in terms of RMSE, CNR and CN and visual examination of the results.

MR patches sampled from the learned distribution shown in Figure 2 support our hypothesis that the VAE model can learn to approximate the distribution of MR patches. The variance maps show that the sulci-like generated structures filled with CSF have higher variance, which is in accordance with the literature [36].

The reconstruction examples in Figure 3 and Figure 4 show that our proposed VAE based reconstruction method produces promising results. This suggests that the learned distribution of MR patches can be used as prior for reconstruction. For  $R=2$  we do not see much of a difference between the fully sampled and reconstructed images, however,  $R=3$  shows limitations of the methods. In this case, the proposed method performs significantly better than the other methods in terms of quality metrics and better or equally in visual quality assessment. As expected, learning the data distribution and using this as a prior works better than enforcing a specific distribution in a specific domain, such as the Laplace distribution in the gradient domain as in TV or more generalized distributions in a kernel domain as in DL. These methods are inherently limited by their formulations compared to the more general formulation of the VAE approach presented here.

Two of the limitations of our method are the variational assumption and the unit Gaussian prior for the latent space. A lot of work went into investigating different latent space prior structures such as Gaussian mixtures or graphical models which could in principal improve the encoding and representative capacity of the latent variables to address the latter limitation [37, 38]. Similarly a lot of research is going into different density estimation methods, for instance using generative adversarial networks [39]. These have the potential to improve on the approximation of the true likelihood and hence to improve reconstruction quality as well.

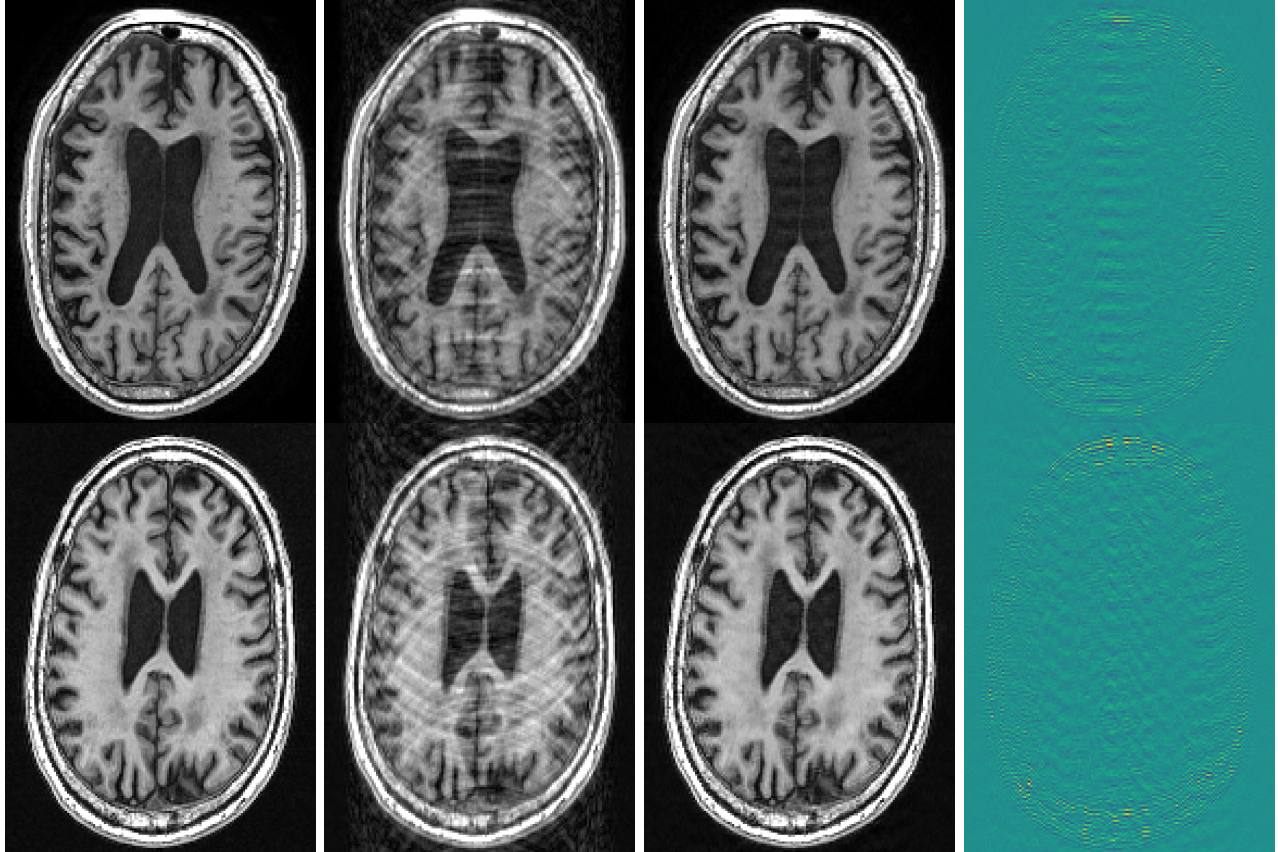
Another limitation of the proposed method is the independence assumption over patches. This assumption can be removed by taking into account the statistical dependence between different patches in an image. However, this is likely to increase the computational complexity of the reconstruction method.

We emphasize the generality of our method in contrast to most methods in the literature. Most DNN based methods require a specific mapping to be learned for every undersampling pattern, whereas our learned priors act on the patches as likelihood measures and are independent of the undersampling strategy used. Our method learns the prior directly on images and can be used to reconstruct any sampling scheme without need of retraining as long as the images are from the same domain.

The ADNI reconstruction results are also encouraging in two terms. First, they show that the learned model does not blur out the lesion regions during the prior projection. Blurring could be expected, since the training images do not have any examples of lesions, however we found that the model can generalize well and incorporate lesions. However, for a proper treatment of images with lesions, we believe the training data set should include images with lesions. We leave creation of such a training set to a future work.

Secondly, the proposed method performs reasonably despite the domain difference between the training and test sets. Although the two data sets are acquired at the same field strength, they still differ in the acquisition protocol and imaging parameters. Furthermore, our method is invariant to FOV changes but not to scale changes. HCP and ADNI voxel sizes are different (1mm x 1mm vs. 1.2 mm x 1 mm), however the reconstructions still look plausible. Notice that the HCP has fat





(a) FS

(b) US

(c) VAE

(d) Error

Figure 5: VAE reconstruction results for two images with white matter lesions due to Alzheimer's disease from the ADNI data set for  $R=2$ . Notice that the VAE is trained only on HCP images from healthy subjects. Images show the original (FS), undersampled (US), reconstructed (VAE) and the error maps from left to right. Lesions are clearly visible in the reconstructed images as well. Error map values are clipped to  $(-0.3, 0.3)$

Table 1: Table summarizing results for different reconstruction quality metrics. Numbers indicate the mean (and standard deviation) of the error metric for N=10 test images. A paired Wilcoxon signed-rank test is used to assess statistical significance with threshold p value chosen as 0.05. The test is performed only between the proposed method and TV and DLMRI methods.

	R=2			R=3		
	RMSE (%)	CNR	CN	RMSE (%)	CNR	CN
FS	-	0.43(0.09)	0.11(0.02)	-	0.43(0.09)	0.11(0.02)
Zero-fill	13.40(0.84)	0.36(0.08)	0.10(0.02)	21.40(1.12)	0.30(0.07)	0.08(0.02)
VAE	2.77(0.39) <sup>†‡</sup>	0.43(0.10) <sup>†‡</sup>	0.11(0.02) <sup>†‡</sup>	4.29(0.51) <sup>†‡</sup>	0.43(0.10) <sup>†‡</sup>	0.11(0.02) <sup>†‡</sup>
TV	4.00(0.51)	0.41(0.10)	0.10(0.02)	7.57(0.71)	0.35(0.10)	0.08(0.02)
DLMRI	4.65(0.54)	0.41(0.10)	0.10(0.02)	7.41(0.83)	0.36(0.10)	0.09(0.02)
ADMMNet	3.74(0.40)	0.43(0.10)	0.11(0.02)	7.49(0.47)	0.39(0.10)	0.10(0.02)

R - net undersampling ratio, RMSE - root mean squared error in percentage, CNR - contrast to noise ratio, CN - contrast, <sup>†</sup>, <sup>‡</sup> indicate statistical significance over the methods TV and DLMRI, respectively.

suppression which reduces the signal from the skull significantly, however ADNI images do not have the suppression, making the dealiasing more challenging. The results indicate that the learned model can to some extent generalize to different scales and imaging protocols without retraining. More challenging problems which might be attacked by domain adaptation methods such as training and testing on different imaging modalities still require further research.

## 6 Conclusion

We presented a novel method for MR reconstruction. The method is based on learning the statistical distribution of MR image patches with VAEs and using it as a prior term for reconstruction from undersampled images.

We have shown that the VAE can approximate the distribution and generate realistic looking MR patches. Furthermore, reconstruction with VAEs yielded promising results for HCP and ADNI data sets in terms of visual quality and quantitative measures.

## Acknowledgements

Authors would like to acknowledge Prof. Klaas Pruessmann and Prof. Sebastian Kozerke for valuable discussions. We thank NVIDIA for their GPU donation. The presented work is funded by Swiss National Science Foundation grant number: 205321\_173016

## References

- [1] D. A. Feinberg, J. D. Hale, J. C. Watts, L. Kaufman, and A. Mark, “Halving mr imaging time by conjugation: demonstration at 3.5 kg.,” *Radiology*, vol. 161, no. 2, pp. 527–531, 1986. PMID: 3763926.
- [2] K. P. Pruessmann, M. Weiger, M. B. Scheidegger, and P. Boesiger, “Sense: Sensitivity encoding for fast mri,” *Magnetic Resonance in Medicine*, vol. 42, no. 5, pp. 952–962, 1999.
- [3] M. Lustig, D. Donoho, and J. M. Pauly, “Sparse MRI: The application of compressed sensing for rapid MR imaging,” *Magnetic Resonance in Medicine*, vol. 58, no. 6, pp. 1182–1195, 2007.

- [4] L. Wissmann, A. Gotschy, C. Santelli, K. C. Tezcan, S. Hamada, R. Manka, and S. Kozerke, “Analysis of spatiotemporal fidelity in quantitative 3d first-pass perfusion cardiovascular magnetic resonance,” *Journal of Cardiovascular Magnetic Resonance*, vol. 19, p. 11, Jan 2017.
- [5] D. L. Donoho, “Compressed sensing,” *IEEE Transactions in Information Theory*, vol. 52, pp. 1289–1306, Apr. 2006.
- [6] E. J. Cands, J. K. Romberg, and T. Tao, “Stable signal recovery from incomplete and inaccurate measurements,” *Communications on Pure and Applied Mathematics*, vol. 59, no. 8, pp. 1207–1223, 2006.
- [7] M. Guerquin-kern, M. Hberlin, K. P. Pruessmann, and M. Unser, “A fast wavelet-based reconstruction method for magnetic resonance imaging,” *IEEE Transactions on Medical Imaging*, pp. 1649–1660, 2011.
- [8] S. G. Lingala, Y. Hu, E. Dibella, and M. Jacob, “Accelerated dynamic MRI exploiting sparsity and low-rank structure: K-t SLR,” *IEEE Transactions on Medical Imaging*, vol. 30, no. 5, pp. 1042–1054, 2011.
- [9] K. P. Pruessmann, M. Weiger, P. Brnert, and P. Boesiger, “Advances in sensitivity encoding with arbitrary k-space trajectories,” *Magnetic Resonance in Medicine*, vol. 46, no. 4, pp. 638–651, 2001.
- [10] H. Pedersen, S. Kozerke, S. Ringgaard, K. Nehrke, and Y. K. Won, “K-t PCA: Temporally constrained k-t BLAST reconstruction using principal component analysis,” *Magnetic Resonance in Medicine*, vol. 62, no. 3, pp. 706–716, 2009.
- [11] J. F. M. Schmidt, L. Wissmann, R. Manka, and S. Kozerke, “Iterative k-t principal component analysis with nonrigid motion correction for dynamic three-dimensional cardiac perfusion imaging,” *Magnetic Resonance in Medicine*, vol. 72, no. 1, pp. 68–79, 2014.
- [12] Y. LeCun, Y. Bengio, and G. Hinton, “Deep learning,” *Nature*, vol. 521, pp. 436–444, May 2015.
- [13] G. Litjens, T. Kooi, B. E. Bejnordi, A. A. A. Setio, F. Ciompi, M. Ghafoorian, J. A. van der Laak, B. van Ginneken, and C. I. Snchez, “A survey on deep learning in medical image analysis,” *Medical Image Analysis*, vol. 42, no. Supplement C, pp. 60 – 88, 2017.
- [14] B. Zhu, J. Z. Liu, B. R. Rosen, and M. S. Rosen, “Neural network mr image reconstruction with automap: Automated transform by manifold approximation,” in *Proceeding of the 25th Annual Meeting of ISMRM*, ISMRM, 2017.
- [15] J. Schlemper, J. Caballero, J. V. Hajnal, A. Price, and D. Rueckert, *A Deep Cascade of Convolutional Neural Networks for MR Image Reconstruction*, pp. 647–658. Cham: Springer International Publishing, 2017.
- [16] Y. Yang, J. Sun, H. Li, and Z. Xu, “Deep admm-net for compressive sensing mri,” in *Advances in Neural Information Processing Systems 29* (D. D. Lee, M. Sugiyama, U. V. Luxburg, I. Guyon, and R. Garnett, eds.), pp. 10–18, Curran Associates, Inc., 2016.
- [17] D. P. Kingma and M. Welling, “Auto-encoding variational bayes,” *CoRR*, vol. abs/1312.6114, 2013.
- [18] D. J. Rezende, S. Mohamed, and D. Wierstra, “Stochastic backpropagation and approximate inference in deep generative models,” in *Proceedings of the 31st International Conference on Machine Learning* (E. P. Xing and T. Jebara, eds.), vol. 32 of *Proceedings of Machine Learning Research*, (Beijing, China), pp. 1278–1286, PMLR, 22–24 Jun 2014.

- [19] S. D. Babacan, R. Molina, and A. K. Katsaggelos, “Bayesian compressive sensing using laplace priors,” *Transactions in Image Processing*, vol. 19, pp. 53–63, Jan. 2010.
- [20] D. P. Wipf and B. D. Rao, “Sparse bayesian learning for basis selection,” *IEEE Transactions on Signal Processing*, vol. 52, pp. 2153–2164, Aug 2004.
- [21] K. P. Murphy, *Machine Learning: A Probabilistic Perspective*. The MIT Press, 2012.
- [22] J. Tsao, P. Boesiger, and K. P. Pruessmann, “k-t blast and k-t sense: Dynamic mri with high frame rate exploiting spatiotemporal correlations,” *Magnetic Resonance in Medicine*, vol. 50, no. 5, pp. 1031–1042, 2003.
- [23] A. Gelman, J. B. Carlin, H. S. Stern, and D. B. Rubin, *Bayesian Data Analysis, Second Edition (Chapman & Hall/CRC Texts in Statistical Science)*. Chapman and Hall/CRC, 2 ed., July 2003.
- [24] C. M. Bishop, *Pattern Recognition and Machine Learning*. Springer, 2006.
- [25] S. Yeung, A. Kannan, Y. Dauphin, and L. Fei-Fei, “Tackling over-pruning in variational autoencoders,” *CoRR*, vol. abs/1706.03643, 2017.
- [26] M. Abadi, P. Barham, J. Chen, Z. Chen, A. Davis, J. Dean, M. Devin, S. Ghemawat, G. Irving, M. Isard, M. Kudlur, J. Levenberg, R. Monga, S. Moore, D. G. Murray, B. Steiner, P. Tucker, V. Vasudevan, P. Warden, M. Wicke, Y. Yu, and X. Zheng, “Tensorflow: A system for large-scale machine learning,” in *12th USENIX Symposium on Operating Systems Design and Implementation (OSDI 16)*, pp. 265–283, 2016.
- [27] A. A. Samsonov, E. G. Kholmovski, D. L. Parker, and C. R. Johnson, “Pocsense: Pocs-based reconstruction for sensitivity encoded magnetic resonance imaging,” *Magnetic Resonance in Medicine*, vol. 52, no. 6, pp. 1397–1406, 2004.
- [28] A. R. De Pierro and E. S. Helou Neto, “From convex feasibility to convex constrained optimization using block action projection methods and underrelaxation,” *International Transactions in Operational Research*, vol. 16, no. 4, pp. 495–504, 2009.
- [29] C. Santelli, M. Loecher, J. Busch, O. Wieben, T. Schaeffter, and S. Kozerke, “Accelerating 4d flow mri by exploiting vector field divergence regularization,” *Magnetic Resonance in Medicine*, vol. 75, no. 1, pp. 115–125, 2016.
- [30] D. P. Kingma and J. Ba, “Adam: A method for stochastic optimization,” *CoRR*, vol. abs/1412.6980, 2014.
- [31] M. F. Glasser, S. N. Sotiropoulos, J. A. Wilson, T. S. Coalson, B. Fischl, J. L. Andersson, J. Xu, S. Jbabdi, M. Webster, J. R. Polimeni, D. C. V. Essen, and M. Jenkinson, “The minimal preprocessing pipelines for the human connectome project,” *NeuroImage*, vol. 80, no. Supplement C, pp. 105 – 124, 2013. Mapping the Connectome.
- [32] M. Reuter, N. J. Schmansky, H. D. Rosas, and B. Fischl, “Within-subject template estimation for unbiased longitudinal image analysis,” *NeuroImage*, vol. 61, no. 4, pp. 1402 – 1418, 2012.
- [33] J. Sled, A. Zijdenbos, and A. Evans, “A nonparametric method for automatic correction of intensity nonuniformity in mri data,” *IEEE Transactions in Medical Imaging*, vol. 17, pp. 87–97, 01 2002.
- [34] M. Uecker, J. I. Tamir, F. Ong, S. Iyer, J. Y. Cheng, and M. Lustig, “Bart: version 0.4.00,” Dec. 2016.

- [35] S. Ravishankar and Y. Bresler, “Mr image reconstruction from highly undersampled k-space data by dictionary learning,” *IEEE transactions on medical imaging*, vol. 30, pp. 1028–41, 11 2010.
- [36] R. Tanno, D. E. Worrall, A. Gosh, E. Kaden, S. N. Sotiropoulos, A. Criminisi, and D. Alexander, “Bayesian image quality transfer with cnns: Exploring uncertainty in dmri super-resolution,” in *Intl Conf. Medical Image Computing and Computer Assisted Intervention (MICCAI)*, Springer, September 2017.
- [37] N. Dilokthanakul, P. A. M. Mediano, M. Garnelo, M. C. H. Lee, H. Salimbeni, K. Arulkumar, and M. Shanahan, “Deep unsupervised clustering with gaussian mixture variational autoencoders,” *CoRR*, vol. abs/1611.02648, 2016.
- [38] M. Johnson, D. K. Duvenaud, A. Wiltchko, R. P. Adams, and S. R. Datta, “Composing graphical models with neural networks for structured representations and fast inference,” in *Advances in Neural Information Processing Systems 29* (D. D. Lee, M. Sugiyama, U. V. Luxburg, I. Guyon, and R. Garnett, eds.), pp. 2946–2954, Curran Associates, Inc., 2016.
- [39] M. Arjovsky, S. Chintala, and L. Bottou, “Wasserstein generative adversarial networks,” in *Proceedings of the 34th International Conference on Machine Learning, ICML 2017, Sydney, NSW, Australia, 6-11 August 2017*, pp. 214–223, 2017.

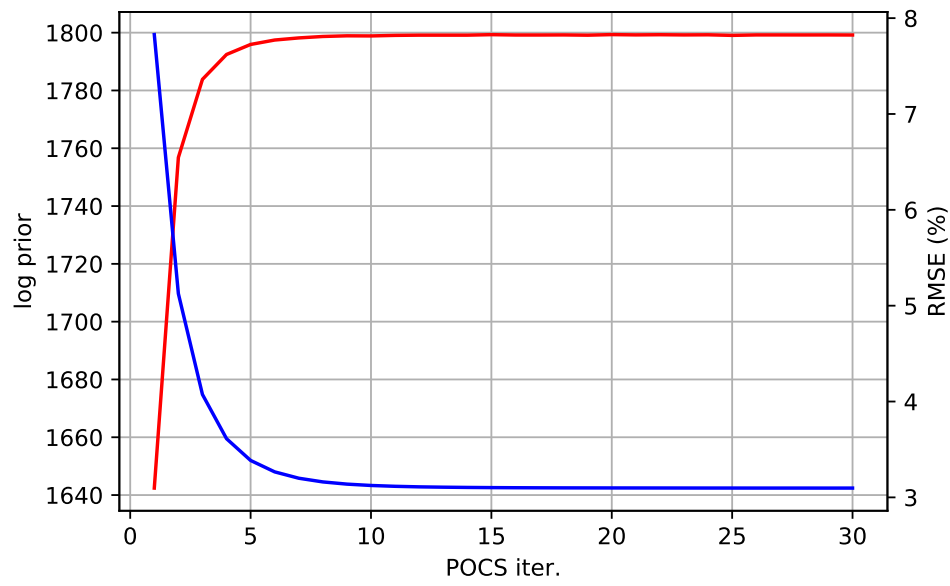


Figure S1: log prior (red) and RMSE (blue) values during POCS reconstruction from an undersampled image with  $R=2$ .

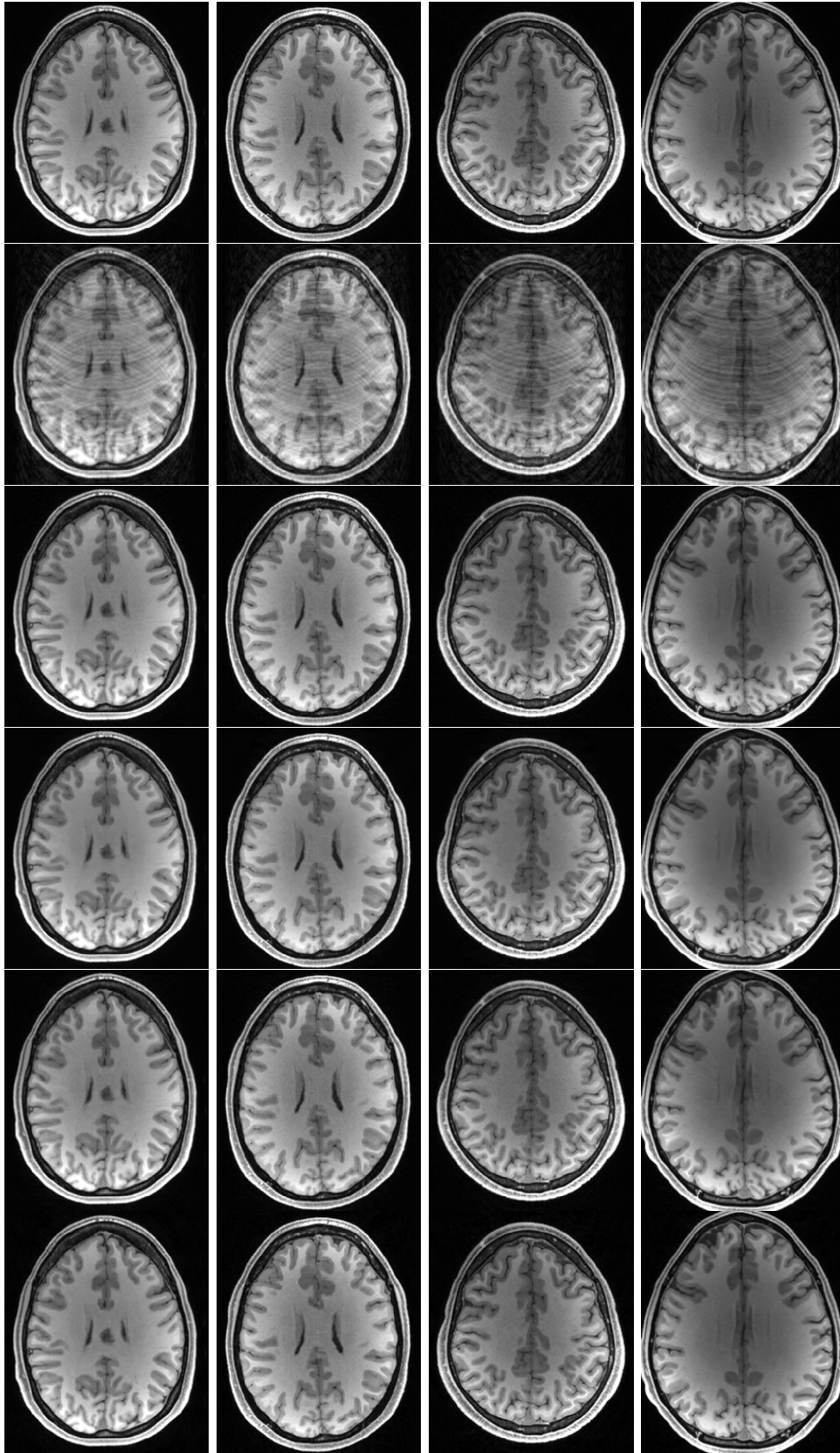


Figure S2: Reconstruction results from 4 different subjects with  $R=2$ . Rows show the original and undersampled images and the VAE, TV, DLMRI and ADMM-Net reconstructions in the up-down direction.

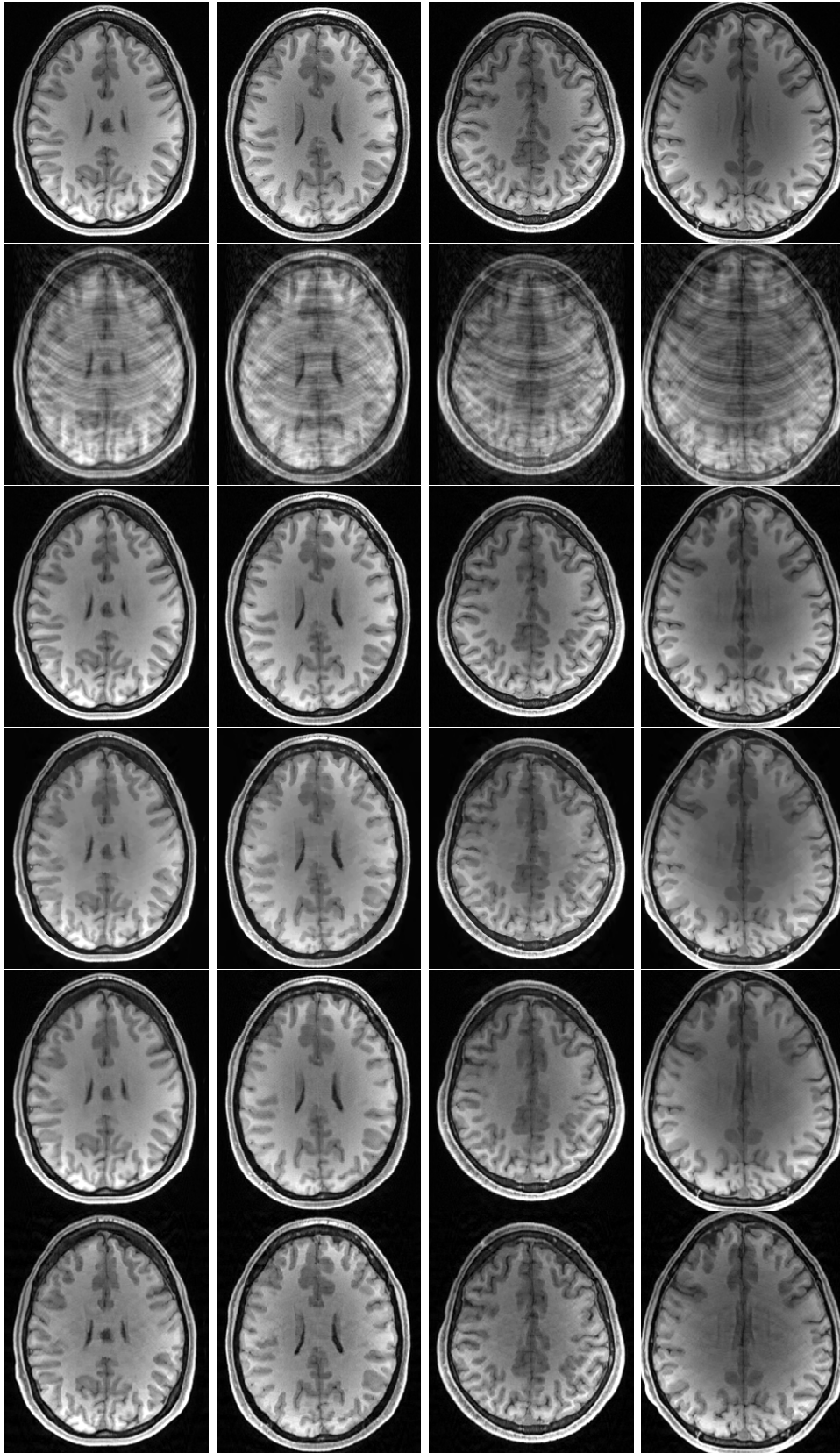


Figure S3: Reconstruction results from 4 different subjects with  $R=3$ . Rows show the original and undersampled images and the VAE, TV, DLMRI and ADMM-Net reconstructions in the up-down direction.